Mobility of daughter elements of 238U decay chain during leaching by In Situ Recovery (ISR): New insights from digital autoradiography

A. Angileri, Paul Sardini, D. Beaufort, G. Amiard, M.F. Beaufort, J. Nicolai, M. Siitari-Kauppi, M. Descostes

Mobility of daughter elements of ^{238}U decay chain during leaching by In Situ Recovery (ISR): new insights from digital autoradiography

A. Angileri[1], P. Sardini[1,*], D. Beaufort[1], G. Amiard[2], M.F. Beaufort[2], J. Nicolai[2], M. Siitari-Kauppi[3] and M. Descostes[4]

[1]IC2MP – Hydrasa, Poitiers University UMR 7285 CNRS, France.

[2]PPRIME, Poitiers University, UPR 3346 CNRS, France.

[3]Radiochemistry Laboratory, University of Helsinki, Helsinki, Finland

[4]Orano Mining, R&D Dpt, Paris, France.

Corresponding author :

Paul Sardini IC2MP, équipe Hydr'ASA

B35, 6 rue Michel Brunet, TSA 51106

86073 Poitiers Cedex 9, France

e-mail : paul.sardini@univ-poitiers.fr

Acknowledgements :

This work was supported by Orano group. We would like to thanks Dr. Claire Fialips (Total Group, Pau, France) for the invaluable help in the use of QEMSCAN device.

Abstract

In highly permeable sedimentary rock formations, U extraction by *in-situ* leaching techniques (ISR – In-Situ Recovery) is generally considered to have a limited environmental impact at ground level. Significantly, this method of extraction produces neither mill tailings nor waste rocks. Underground, however, the outcome for ^{238}U daughter elements in aquifers is not well known because of their trace concentrations in the host rocks. Thus, understanding the *in-situ* mobility of these elements remains a challenge. Two samples collected before and after six months of ISR experiments (Dulaan Uul, Mongolia) were studied with the help of a digital autoradiography technique (DA) of alpha particles, bulk alpha spectrometry, and complementary petrographic observation methods. These techniques demonstrate that before and after leaching, the radioactivity is concentrated in altered and microporous Fe-Ti oxides. Most of the daughter elements of U remain trapped in the rock after the leaching process. DA confirms that the alpha activity of the Fe-Ti oxides remains high after uranium leaching, and the initial secular equilibrium of the ^{238}U series for ^{230}Th to ^{210}Po daughter elements (including ^{226}Ra) of the fresh rocks is maintained after leaching. While these findings should be confirmed by more systematic studies, they already identify potential mechanisms explaining why the U-daughter concentrations in leaching water are low.

Keywords: uranium mining; autoradiograph; in-situ leaching; radium mobility

1. Introduction

In-Situ Recovery (ISR) is a primary method used to extract uranium (U) from porous and permeable rocks. ISR facilities are used to extract U from low-grade ores at lower cost than conventional mining and milling processes (Seredkin et al., 2016). The method consists

of injecting leaching solutions (acidic and/or oxidizing) through a series of wells into the permeable U-mineralized body to dissolve the U-bearing minerals (Habib, 1981; World Nuclear Association, 2018). The leachate is then pumped out through recovery wells and transported to the treatment plant where U is extracted from the mineralized solution. In the absence of a significant amount of carbonate in the reservoir rocks, ISR proceeds by the injection of acidic (sulfuric acid, pH ~ 2) solutions and oxidizing solutions (Eh ~ 0.8 V/SHE) (Robin *et al.*, 2015; Lagneau *et al.*, 2019). This mining technique results in little surface disturbance and generates neither tailings nor waste rock. The restoration of the aquifer is usually performed by 'treat and pump' solutions, in-situ treatment and natural attenuation so as to return it to its initial water classification/quality. Natural attenuation relies on the buffer capacities of the aquifer to attenuate the main contaminants of concern (U, ^{226}Ra and pH) through geochemical processes such as sorption, reduction and precipitation (WoldeGabriel et al., 2014; Gallegos et al., 2015; Robin et al., 2017; Dangelmayr et al., 2018). Currently very few peer-reviewed publications on groundwater restoration at ISR uranium mines are available, especially when acid is used as the leachate (Yazikov and Zabaznov, 2002; Kayukov, 2005; Jeuken et al., 2009; Dong et al., 2016).

The ISR method is based on the geochemical behaviour of uranium which is highly mobile under oxidizing and acidic conditions $U^{(VI)}$ and poorly mobile under reducing conditions $U^{(IV)}$ (Langmuir, 1978; Bourdon et al., 2003). As well as generating the production of a sulfate-rich plume which can contaminate the groundwater beyond the mineralized zones, the use of sulfuric acid as a leachate produces a strong radioactive disequilibrium state in the leached rocks (Lagneau et al., 2019). This disequilibrium is due to the almost total depletion by chemical extraction of the U isotopes which belong to the ^{238}U natural decay chain. Daughter elements are very difficult to investigate due to their very low concentration (ppb-ppt). Understanding the mobility of these radio-elements is an important environmental issue

in the post-mining ISR context. While previous works highlighted the retention of ^{226}Ra by celestine ($SrSO_4$), ilmenite ($TiFeO_3$), barite ($BaSO_4$) and clay minerals (Robin *et al.*, 2017; Lestini et al., 2019; Heberling et al., 2018; Boulesteix et al., 2019; Billon et al., 2020; Besancon et al., 2020), the geochemical behaviour of U-daughter elements is still poorly understood in an acidic context (Déjeant et al., 2016; Déjeant et al, 2014; Chautard et al., 2017; Ballini et al., 2020), in which other important isotopes in the ^{238}U series are ^{230}Th, ^{222}Rn and polonium isotopes (^{218}Po, ^{214}Po, ^{210}Po). As of today, the geochemical studies of U and its daughter elements are based on sequential leaching of the bulk material, which is an expensive, destructive and complex method which is also difficult to interpret (Blanco et al., 2004; Bacon and Davidson, 2008; Menozzi et al., 2016).

A new autoradiographic method for the mapping of alpha particle emissions in geomaterials has been developed very recently (Sardini et al., 2016; Angileri et al., 2018). It is based on the use of a real-time Digital Autoradiograph (DA) device called BeaQuant™. This was initially designed to produce images of beta emissions from medical or biological samples (Donnard et al., 2009a, 2009b, 2009c). More recently, DA has also been employed to map beta emitters in geomaterials (Billon et al., 2019a,b, 2020; Muuri et al., 2019). Compared to existing autoradiographic methods (Illic and Durrani, 2003; Durrani and Illic, 1997; Amgarou, 2002; Siitari-Kauppi, 2002; Cole et al., 2003; Koarashi et al., 2007; Schmidt et al., 2013; Sardini et al., 2015), this digital autoradiograph device provides new type of data. Concerning geomaterials, it is able to spatialize and determine the radioactive equilibrium state of the ^{238}U decay chain on cm-mm scale samples, with a spatial resolution of ~20 µm. The principle is to compare the alpha activity map made by DA and the U-content maps obtained from microprobe analysis (Angileri et al., 2018). The U maps are converted into a theoretical alpha activity map assuming secular equilibrium. Comparing the activities of both

the theoretical and the experimental maps allows us to determine the equilibrium state distribution, and to allocate it in a petrographic framework.

This study is focused on understanding the effects of the mobility of U-series elements in the sands of the geological aquifer at Duulan Uul (Mongolia) after U extraction by the ISR process. In this study we performed a coupled radiometric and mineralogical analysis of two core samples which were extracted from the industrial-scale pilot mining site at Dulaan Uul after a six months of in-situ acidic leaching tests carried out by the ORANO Group (Cardon et al., 2016; de Boissezon et al., 2017). The roll-front mineralization is hosted in Upper Cretaceous sands deposited in a fluviatile to lacustrine environment. One sample is representative of the untreated uranium ore whereas the second one was sampled in the uranium ore which had been subjected to six months of leaching tests.

Investigations were performed by combining bulk alpha spectrometry and multi-scale imaging techniques. On fresh and leached sands, multiscale observations were needed to establish the relationship between the alpha activity and the sand mineralogy. At the scale of the thin section (3×4.5 cm^2), DA was the key technique for the quantitative mapping of alpha activity, and was combined with mineral mapping using QEMSCAN (Quantitative Evaluation of Minerals by SCANning electron microscopy). SEM (Scanning Electron Microscopy) and an electron microprobe were employed at the scale of the primary mineral grains, and TEM (Transmission Electron Microscopy) at the nanometric scale.

Following on from previous studies devoted to ISR process optimization (Bonnaud et al., 2014; Regnault et al., 2014), the main aim of this contribution is to better understand the reactive transport of ultra-trace radioelements of the ^{238}U decay series by combining multi-scale imaging methods of radioactivity and mineralogy.

2. Material and Methods

2.1 Samples

The studied samples were selected after six months of ISR experiments (12/2010 to 06/2011) performed in the U-mineralized sands of the Dulaan Uul site (Mongolia). It consisted of the continuous injection-pumping of a sulphuric acid solution through a pilot extraction cell. During this process, the fluid continuously circulates between the injection and pumping wells in a loop both underground and at the surface. U is extracted from the pumped fluid, whose pH is monitored and readjusted before reinjection in order to maintain its ability to dissolve U in the rock (see Lagneau et al., 2019 for further details). A summarised description of the ISR test is available in Cardon et al. (2016) and de Boissezon et al. (2017). The goal of this experiment was to collect most of the environmental data (variations in pH, water chemistry, mineralogy) needed to determine the effect of the acidic plume in the surrounding aquifer up to several years after the end of acid injection (de Boissezon et al. 2017).

The core samples investigated in this study were collected from two different boreholes drilled at the end of the ISR experiment. Sample F (fresh) was extracted from a depth of 113.10 m and is representative of the uranium ore zone unaffected by the acidic plume. Sample L (leached) was extracted from a depth of 110.80 m and is representative of the uranium ore zone after six months of leaching by acidic solution. This sample came from the same mineralized layer, but the lateral distance between the two core samples is approximatively 30 m (de Boissezon et al. 2017). Such a distance was chosen to guarantee a non-acidic zone. The samples were protected from the atmosphere using airtight bags filled with nitrogen. For both samples, bulk U concentrations were obtained from chemical analysis, and gamma radioactivity was provided by a portable gamma field counter (SPP – Scintillomètre Portatif Prospectif). The data is shown in the “Results” section. Both samples

are mineralogically similar, but we emphasize here that the initial U content of sample L is not accurately known.

2.2 Alpha spectrometry

Alpha spectrometry is a bulk method used here to determine which alpha emitters are present in the studied samples. Measurements were obtained using a CANBERRA A450 PIPS® model with a 450 mm² detector and intrinsic energy resolution (FWHM – Full Width at Half Maximum) of 32 and 26 keV (Radiochemistry Laboratory, University of Helsinki, Finland). The data acquisition and analysis were done with MAESTRO for Windows® Model A65-332 software. The energy calibration was performed with a reference sample containing ^{237}Np (E = 4788 keV, I = 47 %), ^{241}Am (E = 5486 keV, I = 84.5 %) and ^{244}Cm (E = 5805 keV, I = 76.4 %). The distance from the source to the detector was 8.40 ± 0.21 mm. The number of energy channels was 1024. The distance between the sample and the detector window (23.9 mm diameter) was 8.8 ± 0.2 mm. The acquisition time of both samples was set to about one week (614,000 s).

Alpha spectra of thin sections show step-like shapes. This shape is due to the progressive energy loss of the alpha particles emitted through the sample thickness (~30µm); therefore, a well-designed simulation is crucial for analyzing these step-like spectra produced by thick samples. The experimental spectra were adjusted using the 'Advanced Alpha Spectrometry Simulation' (AASI) software (Siiskonen and Pöllänen, 2005)**.** The resulting data enabled the evaluation of the activity of each radionuclide present in the sample. Secular equilibrium is confirmed for a given decay chain if all alpha emitters are present and have the same activity.

2.3 Digital Autoradiography– BeaQuant™

Autoradiography is an imaging technique which provides the spatial distribution of radioactive emissions emerging from a surface. In this contribution, we employed BeaQuant™, which is a real-time digital autoradiograph (DA) system developed by Ai4R SAS (Nantes, France). Compared to older autoradiograph techniques that use films (FA) (Siitari-Kauppi, 2002; Robinet et al., 2015) or phosphor screens (PSA) (Koarashi et al., 2007; Sardini et al., 2015), this device counts particles.

BeaQuant™ is based on the use of micromesh structures such as parallel ionization multipliers working in a proportional mode in a gaseous chamber (PIM - MPGD) (Donnard et al., 2009a, 2009c; Thers et al., 2003). This device was initially designed for analyzing charged particles having a low penetrating power, such as low-energy beta particles emitted by ^{3}H. The gaseous chamber is divided into three parts: amplification, diffusion and reading anode. In these parts are three different electric fields limited by the sample surface, two of micromesh, and the reading anode. Particles emitted by the sample circulate in the gas chamber and interact with the gas, producing electron avalanches. These avalanches occur mainly in the amplification stage and near the sample surface, and they drift into the diffusion part. Amplified avalanches induce sufficiently high voltages above the electronic threshold to be detected by the reading anode.

Contrary to FA or PSA, particles are detected one by one, each particle position being first reconstructed in 2D and then assembled into a raster image. In a given pixel, the intensity represents the number of particles recorded during the exposure time. The acquisition software combined with BeaQuant™ enables the real-time reconstruction and visualization of the amount of radioactive emissions. The chosen amplification system ensures a good spatial resolution; 20 µm for tritium (Donnard et al., 2009b) as well as for alpha particles. The sensitivity of the detector is 5×10^{-4} cpm/mm² (^{3}H), and the maximum counting rate is 3×10^{4} cps in the whole mapped area. Finally, the device is insensitive to X- and gamma rays, which

is a benefit compared to FA and PSA. It is possible to select alpha or beta particles separately by adjusting the BeaQuant™ amplification gains.

The present study used only the alpha mapping capabilities of the BeaQuant™, not the beta ones. In a thick sample containing ^{238}U-series radioelements, the emitted alpha particles are more energetic than the beta particles, which are emitted with very variable and lower energy. Along their path in the gas chamber, alpha particles interact strongly with the gas, mainly in the amplification part. Beta particles also interact mainly in the amplification part, but their energy deposition is significantly lower than for alpha ones. In a previous study, it was estimated that 82% of alpha particles were detected by BeaQuant™ compared to the alpha spectrometry counts (Sardini et al., 2016). As suggested by these authors, a correction factor of 1.22 ± 0.03 was applied to the BeaQuant™ counts. Digital autoradiographs were obtained from two polished petrographic thin sections of F and L samples. These sand samples being homogeneous, just one thin section was sufficient to represent the rock before and after leaching. The total acquisition time was set to 515,200 seconds (~143 h) for both samples. This duration was chosen to ensure the stability of the counting rate in low-activity regions, regardless of the acquisition time. The chosen pixel size for the alpha maps was 20×20 μm^2 which represents a good approximation of the alpha particle range emitted in matter by ^{238}U series emitters. Alpha maps cover the whole thin-section surface for both studied samples.

The alpha emission autoradiographs obtained for both studied samples contain areas of high and concentrated alpha activity, referred to as “hotspots” hereafter. Areas of low activity (the matrix between the hotspots) are referred to as “diffuse areas” hereafter (see section 3.1). Angileri et al. (2018) observed similar patterns from crushed ore and fresh uranium mill tailings. Because hotspots are related to the mineralogy of the sand (see section 3.1), we made a special focus on the characterization of hotspot activity at the thin-section scale. The total activity of the hotspots and diffuse areas was determined; we were also able to analyze the

hotspots individually by processing the autoradiographic images, using segmentation (Figure S1, supplementary material), and a spot-by-spot analysis. The latter consists of (1) the determination of total alpha activity emitted by each spot and (2) the determination of the area of each spot in 2D. The total activity of a given spot is obtained by superimposing the binary image of the spots onto the raw alpha map, and by integration of the spot activity. The area of a given spot is equal to its number of pixels multiplied by the pixel size (here 20×20 μm^2). Image processing and analysis procedures were performed using the imaging software Aphelion™.

2.4 Mineral mapping

SEM-EDS QEMSCAN, a non-destructive Scanning Electron Microscopy (SEM) method using Energy Dispersive X-Ray Spectroscopy (EDS), was used to produce 2D elemental and mineralogical maps of the thin sections. The acquisitions were performed using an FEI FEG-SEM QEMSCAN 650F electron microscope (Total S.A., Pau, France) with an accelerating voltage of 15 kV and a beam current of 10 nA. The main aim here was to clarify the relationship between the mineralogy and the alpha activity hotspots using mineral maps acquired at the same scale as the alpha maps. Firstly, SEM-EDS QEMSCAN provided the Back-Scattered Electrons (BSE) images and Elementary maps (Na, Mg, Al, Si, P, S, K, Ca, Ti, Mn, Fe, Zr, Ba, U) of the carbon-coated thin sections. The pixel size of the EDS analyses was about 15 µm. BSE images were acquired with a resolution of 586 nm. The 2D SEM-EDS elemental maps were then post-treated using a dedicated Spectral Analysis Engine (SAE) developed by FEI, called Nanomin, allowing the automatic 2D quantification of the mineralogy by the deconvolution of the mixed X-ray spectra of each analyzed pixel using up to three reference mineral spectra. The reference mineral spectra are selected from a dedicated database or measured on pure mineral grains by a specialist.

SEM-EDS QEMSCAN's chemical and mineralogical maps were manually superimposed onto Beaver™ alpha activity maps to locate the activity spots in the SEM-EDS QEMSCAN images. Any global SEM-EDS QEMSCAN map is made of several smaller sub-images which are easier to handle than a larger global map, which is in fact a large composite image. A total of six (sample F) and eleven (sample L) spots were randomly selected as ROI (Regions of Interest) in the alpha maps and located on the related mineralogical maps. SEM-EDS QEMSCAN elementary maps are 8-bit raster images whose intensities are proportional to the atomic percentage. In the present study, the thin-section scale maps from SEM-EDS QEMSCAN were only used for a qualitative mineral recognition of the hotspots. The purpose here was not to extract mass contents from the EDS analyses, which would require tedious calibration with reference quantitative mineralogical analyses performed on the crushed samples (Fialips et al., 2018).

To accurately determine the mass contents, an electron microprobe analysis was used, in point analysis mode or mapping mode. Because this analysis technique is more cumbersome, it was focused on the hotspots and the chemical concentrations maps obtained in thin sections were performed at the scale of 0.1 to 1 mm. Microchemical analyses were performed using an electron microprobe equipped with a wavelength dispersive spectrometer (model CAMECA SX-FIVE) in the CAMPARIS facility, Pierre et Marie Curie University, Paris. An acceleration voltage of 15 keV, a count time of 180-240 seconds, and a probe current of 15 nA were selected for Si, P, Ca, Fe, Ti, Al, Mg, Na, K, Mn, and Pb. Note that Ra mapping is not possible using either QUEMSCAN or microprobe, as the Ra content is 3×10^6 lower than the ^{238}U content (it is an ultra-trace element). The probe current was fixed at 150 nA for U and Th, the detection limit was estimated as 100–200 ppm, with the interaction volume of the beam around 5 µm (Goldstein et al., 2007). The bulk U content of the F and L samples (180 and 6 ppm respectively) is concentrated in mineral grains having an internal content of U

which is higher than the provided detection limit. The chemical maps were acquired at 15 keV with a probe current of 298 nA. Chemical mapping acquisition was made using a 2 µm step length, a dwell of 0.1 second, and the detection limit of U was estimated to be around 0.2% (2000 ppm).

2.5 Small scale observations

Thin cross-sections for TEM analysis were prepared by the FIB/SEM (Focused ion beam / Scanning electron microscope) method with a FEI-HELIOS dual-beam G3 using the standard lift-out method (Giannuzzi and Stevie (1999), Langford and Clinton (2004). This instrument, available at the PPrime Institute, incorporates electron- and ion-beam columns. The liquid-metal ion source (LMIS) is gallium. Four thin cross-sections were prepared, two for each sample. Their size is approximatively 15×10 µm² with a thickness lower than 150 nm for specific EDS analysis. We observed and analyzed the mineral heterogeneity of the hotspots at high resolution.

FIB is equipped with an EDS detector from EDAX SDD (Silicon Drift Detector); a 15 keV beam was used to detect all the elements present in the samples. At this acceleration voltage the probe size is smaller than 10 nm, which results in a very good spatial resolution during the EDS analysis. We used those chemical analyses to end-point the position of the lamella for the TEM analysis.

Chemical analysis and petrographic observations were made using high-angle annular dark-field scanning transmission electron microscopy (HAADF-STEM). HAADF-STEM imaging is a mapping technique based on the detection of incoherent electrons elastically scattered by the sample at a high angle. The resulting image contrast is related to the atomic number and provides a chemical analysis of the nano-particles (Howie, 1979; Pennycook and Jesson,

1991). HAADF-STEM observation and analysis were performed with a Jeol 2200FS FEG TEM operating at 200keV. The microscope is equipped with a Bruker EDS SDD detector.

3. Results and Discussion

3.1 Petrographic observations and digital autoradiograph of alpha activity

The core samples are poorly-consolidated to unconsolidated, medium- to coarse-grained arkosic sands. Each core sample consists of poorly sorted angular material made of lithic fragments and detrital minerals. Lithic fragments are composed of granitoids (granite, pegmatite) with subordinate volcanic rocks (rhyolite, andesite). The detrital mineral assemblage comprises quartz, alkali feldspars (microcline, orthoclase and albite) and phyllosilicates, which are made up of white micas, chlorite, biotite and smectite. Accessory minerals were mainly pyrite, epidote, tourmaline, zircon and polycrystalline grains consisting of various types of Fe-Ti minerals (ilmenite, Ti-magnetite, rutile, anatase and titanite). The primary porosity of the sandy sediments is partly filled by a fine-grained polycrystalline sedimentary matrix having the same mineralogical composition as the coarse-grained detrital assemblage. At a higher magnification, all the detrital grains (except the quartz) present evidence of dissolution and partial replacement by clay minerals (montmorillonite). In the F sample, U-mineralization consists mainly of uraninite with two specific crystal habits: (1) minor amounts of individual uraninite crystals distributed within the lithic fragments and (2) a covering of the dissolution surface of Fe-Ti and Ti minerals (Ti -magnetite, ilmenite, rutile, titanite, anatase) with large amounts of uraninite nanograins (50 to 100 nm in diameter) and a partial infilling of the residual pore space with montmorillonite (Figure 1). TEM observations show that uraninite nanograins are polycrystalline, and made up of aggregates of uraninite nanocrystals (Figure 1).

From a mineralogical point of view, the sands of the L sample differs from those of the F sample by the total disappearance of uraninite and a strong dissolution of pyrite (Figure 2). An SEM/EDX analysis on both samples of the Fe-Ti minerals (Figure S2, supplementary material) and a detailed TEM observation of the latter's alteration sites confirms the total disappearance of uraninite nanograins and the absence of crystallization of secondary minerals at any scale of observation (Figure 2).

A bulk characterization of the samples in terms of U-concentration and Ra/U activity ratio was first performed. A U-concentration of 383 ppm and a Ra/U activity ratio of 0.7 indicating the radioactive equilibrium of the ^{238}U series were measured in the bulk sample F (^{226}Ra activity is 3.34 Bq/g). A very low U-concentration (6 ppm) and a very high Ra/U activity ratio (29) were measured in bulk sample L, indicating a strong radioactive disequilibrium of the ^{238}U series after uranium leaching (^{226}Ra activity is 2.18 Bq/g). The persistence of radio-elements of the ^{238}U decay chain in the leached mineralized sands is confirmed by the field gamma counter analysis which indicates that despite almost complete leaching of the uranium (6 ppm in sample L vs 383 ppm in sample F), the radioactivity remains high in sample L after the leaching test (100 cps for L sample against 133 cps for F sample, respectively).

Digital alpha autoradiographs acquired for both samples display a similar heterogeneous spatial distribution of alpha activity, presenting scattered hotspots (Figure 3). However, larger hotspots were observed in the F sample. For the L sample, considering the very low residual uranium content (6 ppm) and the total dissolution of uraninite nanograins after acidic leaching, finding hotspots in the images is an unexpected result which indicates the persistence of a significant alpha activity of alpha-emitting radionuclide(s) other than uranium.

From the superimposition of the mineralogical maps obtained by QEMSCAN onto the alpha map of the same area obtained by DA (Figure S3, supplementary material), we see that the

hotspots identified in both samples are mostly located in the aggregates of Fe-Ti minerals as described above.

Such observations have already been made in the same geological context (namely the South Tortkuduk roll-front deposit in Kazakhstan) (Boulesteix et al., 2019). Chemical maps of Fe-Ti minerals of the L sample obtained from microprobe analysis (WDS X-ray spectrometry) confirm the almost total depletion of uranium after acidic leaching (Figure S4, supplementary material). The uranium content never exceeds 0.2 wt% in the leached Fe-Ti minerals of sample L while it commonly exceeds 30 wt% in unleached Fe-Ti minerals. The only significant traces of uranium persisting locally within the leached aggregates of Fe-Ti minerals (0.2 wt%) are potentially related to minute grains of zircon. For both samples the presence of light chemical elements such as Al, Si, Na and Mg is related to smectite minerals which do not seem particularly well dissolved after the acidic leaching process (Robin et al., 2016; Robin et al., 2020).

3.2 Alpha spectrometry

Alpha spectrometry analyses were also performed to confirm the equilibrium state of the ^{238}U decay chain in both samples. Because alpha emission occurs in the thickness of the samples, alpha spectra are “step-like”. Table 1 shows the calculated contribution of each radionuclide in the alpha simulated spectra using AASI (Advanced Alpha Spectrometry SImulation) software (Siiskonen and Pöllänen, 2005).

The spectrum of the F sample shows the presence of alpha emitters of the whole ^{238}U decay chain (Figure 4). All emitters present the same contribution in the simulation, indicating secular equilibrium for this sample (Ra/U ~ 1). The L sample shows the absence of ^{238}U and ^{234}U energy peaks, indicating global disequilibrium of the decay chain. Moreover, the AASI simulation shows the same activity contribution for the remaining daughter elements,

indicating local equilibrium in the decay chain from ^{230}Th to ^{210}Po. The low activity of the L sample makes the spectrum quite noisy. Accurate determination of Ra/U ratio is not possible here because the U steps are below the detection limit.

3.3 Bulk alpha activity from alpha autoradiograpy

Previous work shows that alpha maps acquired by BeaQuant™ device are quantitative (Sardini et al., 2016). The alpha activity of the leached sample (2.3×10^{-4} cps/mm²) is around four times lower than in the fresh sample (9.3×10^{-4} cps/mm²). For both samples a theoretical activity assuming secular equilibrium was calculated based on their bulk U content (see section 3.1). The theoretical activities of the F and L samples are 7×10^{-4} cps/mm² and 1.3×10^{-5} cps/mm², respectively. The ratio R = theoretical alpha activity / measured alpha activity is 0.77 and 0.055 for the F and L samples, respectively. These ratios indicate a secular equilibrium for the fresh sample (R~1), and a strong disequilibrium, with a lack of U (R <<1) for the leached sample. Such a calculation enables an approximation of the bulk equilibrium state of both samples without using spectrometry. When alpha spectrometry and BeaQuant™ are combined, estimations of ^{226}Ra activities give 8.6 and 2.8 Bq/g in samples F and L respectively. These two activities are close to the ones estimated by bulk methods (see section 3.1), but the ^{226}Ra activity of the F sample measured in the studied thin section is larger.

3.4 Analysis of hotspot activity

The alpha map observation enables us to identify and spatialize the alpha activity (Figure 3). Total activities are normalized to the related window area. For the F and L samples, 131 and 111 spots were analyzed, and the area of the spots was measured to be 1.2% and 0.8% of the total area of the ROIs, respectively. So the spot areas are quite low compared to the total ROI area.

On the F sample, the alpha activity emitted by the hotspots is 1.81×10^{-2} cps/mm² (total spot activity divided by total spot area). On the L sample, the total activity emitted from the hotspots is 1.23×10^{-2} cps/mm². The hotspot activity is quite comparable before and after leaching. We emphasize that this hotspot activity is high compared to the bulk, as it corresponds to 25% and 28% of the whole sample's activity, respectively for the F and L samples. These contributions are calculated taking into account the total area of the hotspots. The average activity emitted by a hotspot (total spot activity [cps] divided by spot number) is 1.17×10^{-3} cps for the F sample, and 0.49×10^{-3} cps for the L sample. These activities are determined from all hotspots, regardless of spot size.

After segmentation of the hotspots, it was possible to extract the size (mm^2) and the activity (cps) of each spot, so as to perform an individual analysis of each hotspot. Figure 5 is a plot diagram where each spot is shown using its own size and activity, one point representing one spot. The expected behaviour was that the larger the spot, the higher its activity. Such an expectation was verified (Figure 5). However, several important additional observations can be made: (1) for a given spot size, there is no difference of activity between both samples, and (2) the F sample contains larger spots than the L sample, seven spots of the F sample having an activity higher than 4×10^{-3} cps.

Moreover, there is a good correlation between the size and the activity of the spot in both samples. On a log-log scale, a linear trend between spot activity and spot size is observed for both samples. If the big spots of the F sample are excluded, the adjustment of the point cloud gives a similar result for both samples: $A = A_0 \times size^m$. Such a linear behaviour indicates that spot activity and spot size are linked by a power law. The A_0 term represents the activity for a grain size = 1 mm^2 (A_0 is nearly 0.03 cps here for both samples) and m is the power factor of the adjustment law. The obtained power factors are very similar for both samples (m ~ 1.3). This relationship suggests a kind of "fractal behaviour" of the alpha activity according to the

hotspot size. Determination of the Fe-Ti oxide masses linked to each spot would certainly have enabled a better understanding of the relationship. However, the fractal behaviour suggests an effect of fractal geometry of the grains. This will be investigated in further studies.

3.5 Implication for the mobility of ^{238}U daughters elements

The use of the ISR method is increasing in the mining industry, especially for U extraction. This is mainly due to its capability to drastically reduce production costs and its low impact on the surface environment compared to conventional mining methods (Seredkin et al., 2016). Nevertheless, important questions persist about the global/underground environmental impact of this technique. The main goal of this work was to develop a new quantitative approach coupling complementary and multiscale mapping methods to better understand the influence of the mineral framework on the mobility of radioactive elements.

Petrographic observations reveal that the alpha activity of spots which persist after almost total leaching of uranium from the bulk rock is located in aggregates of altered Fe-Ti minerals (ilmenite, anatase, rutile, titanite) with a large internal and open porosity (with a pore size observed by TEM ranging from micrometer to nanometer). STEM-HAADF analysis of ultrathin sections showed the chemical complexity of these mineral assemblages with quite varying Fe and Ti contents, and the presence of smectite in the microporous network.

DA indicates that leaching has a limited influence on spot activity, because, comparing the F and L samples: (1) the contribution of spot activity to total activity is similar, and (2) the activities of spots having the same size are similar. As only two U isotopes were removed, spots of the leached sample would emit three quarters of the initial spot activity in the fresh sample. We did not observe such a difference in spot activity in the two samples: for a given spot size, we measured a comparable activity (Figure 4). Such a discrepancy may be due to

the difference of initial U concentrations of spots in the two samples: the fresh sample can be considered as an initial state of the leached one, but only from a mineralogical point of view. Finally, the most important fact to remember here is the low variation of individual spot activity, suggesting that the leaching process of U was homogeneous in the sand but that daughter elements from ^{230}Th to ^{210}Po still persist in the Fe-Ti minerals after leaching. A similar conclusion can be proposed for the radioactively diffuse area. The activity of the diffuse area is not attributed to a specific mineralogy, but corresponds to the whole mineralogy of the sample. It was not possible to link this diffuse activity to the mineralogy, because this activity is spread across this region, without any "clustering". Possibly, in the fresh rock, this activity comes from tiny uraninite grains dispersed in the sand. In the bulk leached rock, the activity of the diffuse area comes also from ^{230}Th to ^{210}Po, but contrary to hotspots, the mineral phase(s) are not detected. The weak and dispersed activity in this region prevents us from assigning a mineral phase for these radio-elements. However, the ratio of spot activity to global activity is similar for both samples (nearly 25%), suggesting no selectivity of the leaching in hotspots and in the diffuse area. The absolute difference of activity between the F and L samples could be explained by a variation of the initial U content on both samples, affecting hotspots and diffuse area activities similarly.

The alpha spectrometry results support these conclusions, because the initial secular equilibrium of the ^{238}U chain (in sample F) is measured and maintained for ^{230}Th to ^{210}Po daughter elements in sample L. Such observations agree with the environmental data survey for ^{226}Ra (de Boissezon et al., 2017; Lagneau et al., 2019). It appears that Fe-Ti minerals constitute an efficient trap for the "undetectable" U daughters. Such an observation seems consistent considering the reactivity of an altered ilmenite surface such as hydrous ferric oxides, known for their retention capacities of ^{226}Ra (Ames et al., 1983; Sajih et al., 2014) and

the high cation exchange capacity of the smectites (Robin et al., 2017) located in the microporous space.

4. Conclusion

In the ISR context, this study managed to develop a new quantitative multi-scale approach by combining complementary methods in order to better understand the influence of mineralogy on the mobility of radioactive elements which are difficult to detect. A digital autoradiography technique was employed; it is a relatively inexpensive and straightforward imaging technique that can be easily combined with mineralogical maps and petrographical investigations. Our findings suggest a limited migration of the U decay product from the ISR cell of the Dulaan Uul site, consistent with a natural attenuation process. Potential mechanisms were identified, explaining why the U-daughter concentrations in leaching water are low. To evaluate the environmental impact of these results, further studies are however required, by investigating more statistically the leaching of the sand, by increasing the number of studied samples, and by following the hydro-chemistry of water near the ISR cells. More generally, this work provides a new approach for understanding the mobility of the U decay products which could be applied to U-mining sites worldwide and to leaching lab experiments where initial conditions are better controlled.

References

Ames, L.L., McGarrah, J.E., Walker, B.A., Salter, P.F., 1983. Uranium and radium sorption on amorphous ferric oxyhydroxide. Chem. Geol. 40 (1–2), 135–148. DOI 10.1016/0009-2541(83)90095-5.

Amgarou, K., 2002. Long-term measurements of indoor radon and its progeny in the presence of thoron using nuclear track detectors. A novel approach, PhD Dissertation, Barcelona, 2002.

Angileri, A., Sardini, P., Donnard, J., Duval, S., Lefeuvre, H., Oger, T., Patrier, P., Rividi, N., Siitari-Kauppi, M., Toubon, H., Descostes, M., 2018. Mapping 238U decay chain equilibrium state in thin sections of geo-materials by digital autoradiography and microprobe analysis. Appl. Radiat. Isot. 140, 228–237. DOI 10.1016/j.apradiso.2018.06.018.

Bacon, J., Davidson, C., 2008. Is there a future for chemical extraction? Analyst 133, 25–46.

Ballini, M., Nos, J., Phrommavanh, V., Descostes, M., 2017. U and 226Ra mobility in the uranium mill tailings of Bellezane (France), Goldschmidt Conference, Paris, France.

Ballini, M., Chautard, C., Nos, J., Phrommavanh, V., Beaucaire, C., Besancon, C., Boizard, A., Cathelineau, M., Peiffert, C., Vercouter, T., Vors, E., Descostes, M., in press. A multi-scalar study of the long-term reactivity of Uranium mill tailings (Bellezane, France). J. of Env. Radioact.

Besancon, C., Chautard, C., Beaucaire, C., Savoye, S., Sardini, P., Gérard, M., Descostes M., accepted 2020. Modeling the role of barite in the limitations of sequential extractions used to localize Radium 226 in geo-samples. Minerals.

Billon, S., Sardini, P., Leblond, S., Fichet, P., 2019a. From Bq/cm^2 to Bq/cm^3 (and conversely) - Part 1: a useful conversion for autoradiography, J. of Radioanal. Nuc. Chem. DOI 10.1007/s10967-019-06521-w.

Billon, S., Sardini, P., Leblond, S., Fichet, P., 2019b. From Bq/cm^2 to Bq/cm^3 (and conversely) - Part 2: a useful conversion for decommissioning activities, J. of Radioanal. Nuc. Chem. DOI 10.1007/s10967-019-06540-7.

Billon, S., Sardini, P, Angileri, A. Beaucaire, C. Parneix, J-C., Siitari-Kauppi, M. Descostes, M., 2020. Quantitative imaging of ^{226}Ra ultratrace distribution using electronic autoradiography: case of doped celestines. J. of Env. Radioact. 217, 106211.

Blanco, P., Tomé, F., Lozano, J., 2004. Sequential extraction for radionuclide fractionation in soil samples: a comparative study. Low Level Radionucl. Meas. Tech. - ICRM 61 (2), 345–350. DOI 10.1016/j.apradiso.2004.03.006.

Bonnaud, E., Lagneau, V., Regnault, O., Fiet, N., 2014. Reactive transport simulation of uranium ISR: effect of the density driven flow, in: Proceedings of the 7th International Conference on Uranium Mining and Hydrogeology, Freiberg, Germany.

Boulesteix, T., Cathelineau, M., Deloule, E., Brouand, M., Toubon, H., Lach, P., Fiet, N., 2019. Ilmenite and their alteration products, sinkholes for uranium and radium in roll-front deposits after the example of south Tortkuduk (Kazakhstan). J. of Geochem. Explo. 206. DOI 10.1016/j.gexplo.2019.106343.

Bourdon, B., Turner, S., Henderson, G.M., Lundstrom, C.C., 2003, Introduction to U-series geochemistry, in: Bourdon, B. et al. (eds.), Review in Mineralogy and Geochemistry, Uranium-Series Geochemistry. Mineralogical Society of America, Washington. 52, 1–21.

Cardon, O., Le Goux F., Salabert, J., 2016. Prospection d'uranium en Mongolie: découverte majeure dans le désert de Gobi [Uranium exploration in Mongolie: important discovery in the Gobi desert]. Rev. Générale Nucléaire, 47.

Chautard, C., Beaucaire, C., Gérard, M., Phrommavanh, V., Nos, J., Galoisy, L., Calas, G., Roy, R., Descostes, M., 2017. Geochemical characterization of U tailings (Bois Noirs Limouzat, France). Procedia Earth Planet. Sci. 17, 308–311. DOI 10.1016/j.proeps.2016.12.067.

Cole, J. M., Nienstedt, J., Spataro, G., Rasbury, E. T., Lanzirotti, A., Celestian, A. J., Nilsson, M., Hanson, G. N., 2003. Phosphor imaging as a tool for in situ mapping of ppm levels of uranium and thorium in rocks and minerals. Chem. Geol. 193 (1), 127–136. DOI 10.1016/S0009-2541(02)00223-1.

Dangelmayr, M.A., Reimus, P., Johnson, R.H., Clay, J.T., Stone, J.J., 2018. Uncertainty and variability in laboratory derived sorption parameters of sediments from a uranium in situ recovery site. J. Contam. Hydrol. 213, 28–39. DOI 10.1016/j.jconhyd.2018.04.001.

de Boissezon, H., Levy, L., Jakymiw, C., Descostes, M., 2017. Remediation of a uranium acidic in situ recovery mine: from laboratory to field experiments using reactive transport modelling. in: Proceedings of the 16th International Conference on the Chemistry and Migration Behaviour of Actinides and Fission Products in the Geosphere, Barcelona, Spain.

Déjeant, A., Galoisy, L., Roy, R., Calas, G., Boekhout, F., Phrommavanh, V., Descostes, M., 2016. Evolution of uranium distribution and speciation in mill tailings, COMINAK mine, Niger. Sci. Total Environ. 545–546, 340–352. DOI 10.1016/j.scitotenv.2015.12.027.

Déjeant, A., Bourva, L., Sia, R., Galoisy, L., Calas, G., Phrommavanh, V., Descostes, M., 2014. Field analyses of 238U and 226Ra in two uranium mill tailings piles from Niger using portable HPGe detector. J. Environ. Radioact. 137, 105–112. DOI 10.1016/j.jenvrad.2014.06.012.

Dong, Y., Xie, Y., Li, G., Zhang, J., 2016. Efficient natural attenuation of acidic contaminants in a confined aquifer. Environ. Earth Sci. 75(7), 595. DOI 10.1007/s12665-016-5389-8.

Donnard, J., Arlicot, N., Berny, R., Carduner, H., Leray, P., Morteau, E., Servagent, N., Thers, D., 2009a. Advancements of labelled radio-pharmaceutics imaging with the PIM-MPGD. J. Instrum. 4 (11), 11022–11022. DOI 10.1088/1748-0221/4/11/P11022.

Donnard, J., Thers, D., Servagent, N., Luquin, L., 2009b. High spatial resolution in beta-imaging with a PIM device. IEEE Trans. Nucl. Sci. 56 (1), 197–200. DOI 10.1109/TNS.2008.2005673.

Donnard, J., Berny, R., Carduner, H., Leray, P., Morteau, E., Provence, M., Servagent, N., Thers, D., 2009c. The Micro-Pattern Gas Detector PIM: a multi-modality solution for novel investigations in functional imaging. Nucl. Instrum. Methods Phys. Res. Sect. Accel. Spectrometers Detect. Assoc. Equip. 610 (1), 158–160. DOI 10.1016/j.nima.2009.05.186.

Durrani, S. A., Illic, R., 1997. Radon measurements by etched track detectors - application in radiation protection, Earth Sciences. World Scientific Publishing Company.

Fialips, C., Labeyrie, B., Burg, V., Mazière, V., Munerel, Y., Haurie, H., Jolivet, I., Lasnel, R., Laurent, J.-P., Lambert, L., Jacquelin-Vallée, L., 2018. Quantitative Mineralogy of Vaca Muerta and Alum Shales From Core Chips and Drill Cuttings by Calibrated SEM-EDS Mineralogical Mapping. In : URTeC 2018, Unconventional Resources Technology Conference, Houston, USA.

Gallegos, T.J., Campbell, K.M., Zielinski, R.A., Reimus, P., Clay, J.T., Janot, N., Bargar, J.R., Benzel, W.M., 2015. Persistent U(IV) and U(VI) following in-situ recovery (ISR) mining of a sandstone uranium deposit, Wyoming, USA. Appl. Geochem. 63, 222–234. DOI 10.1016/j.apgeochem.2015.08.017.

Giannuzzi L.A., Stevie, F.A., 1999. A review of focused ion beam milling techniques for TEM specimen preparation. Micron 30, 197–204.

Goldstein, J., Newbury, D., Joy, D., Lyman, C., Echlin, P., Lifshin, E., Sawyer, L., Micheal, J., 2007. Scanning Electron Microscopy and X-Ray microanalysis, 3th ed. Springer, Berlin.

Habib Jr, H.T., 1981. Process for in-situ leaching of uranium, Google Patents.

Heberling, F., Metz, V., Böttle, M., Curti, E., Geckeis, H., 2018. Barite recrystallization in the presence of 226Ra and 133Ba. Geochem. Cosmo. Acta. 232. DOI 10.1016/j.gca.2018.04.007.

Howie, A., 1979. Image contrast and localized signal selection techniques. J. Microsc. 117 (1), 11–23. DOI 10.1111/j.1365-2818.1979.tb00228.x.

Illic, R., Durrani, S. A., 2003. Solid state nuclear tracks detectors, in: L'Annunziata, M.F. (Ed.), Handbook of Radioactivity Analysis. Elsevier, Amsterdam; pp 179–237.

Jeuken, B., Kalka, H., Maerten, H., Nicolai, J., Woods, P., 2009. Uranium ISR mine closure – general concepts and model-based simulation of natural attenuation for south australian mine sites, in : URAM-2009, International Symposium on Uranium Raw Material for the Nuclear Fuel Cycle, IAEA, Vienna, Austria.

Kayukov, P., 2005. APPENDIX VI. Kanzhugan environmental rehabilitation after closure, in: IAEA Technical report IAEA-TECDOC-1428, Guidebook on environmental impact assessment for in situ leach mining projects, pp 101–117.

Koarashi, J., Saito, F., Akiyama, K., Rahman, N.M., Iida, T., 2007. A new digital autoradiographical method for identification of Pu particles using an imaging plate. Appl. Radiat. Isot. 65 (4), 413–418. DOI 10.1016/j.apradiso.2006.07.016.

Lagneau, V., Regnault, O., Descostes, M., 2019. Industrial Deployment of Reactive Transport Simulation: an Application to Uranium in situ Recovery. Reviews in Mineralogy and Geochemistry 85, 499-528.

Langford, R.M., Clinton, C., 2004. In situ lift-out using a FIB-SEM system, Micron 35(7), 607–611. DOI 10.1016/j.micron.2004.03.002.

Langmuir, D., 1978. Uranium solution-mineral equilibria at low temperatures with applications to sedimentary ore deposits. Geochim. Cosmochim. Acta 42, 547–569. https://doi.org/10.1016/0016-7037(78)90001-7.

Lestini L., Beaucaire C., Vercouter T., Ballini M., Descostes M., 2019. Role of trace elements in the 226-Radium incorporation in sulfate minerals (gypsum and celestite). ACS Earth Space Chemistry. 3(2), 295–304. DOI 10.1021/acsearthspacechem.8b00150.

Menozzi, D., Dosseto, A., Kinsley, L.P.J., 2016. Assessing the effect of sequential extraction on the uranium-series isotopic composition of a basaltic weathering profile. Chem. Geol. 446, 126–137. DOI 10.1016/j.chemgeo.2016.05.031.

Muuri, E., Sorokina, T., Donnard, J., Billon, S., Helariutta, K., Koskinen, L., Martin, A., Siitari-Kauppi, M., 2019, Electronic autoradiography of ^{133}Ba particle emissions; diffusion profiles in granitic rocks. App. Rad. Isotopes. 149,108–113. DOI 10.1016/j.apradiso.2019.04.026

Pennycook, S.J., Jesson, D.E., 1991. High-resolution Z-contrast imaging of crystals. Ultramicroscopy. 37 (1–4), 14–38. DOI 10.1016/0304-3991(91)90004-P.

Regnault, O., Lagneau, V., Fiet, N., 2014. 3D reactive transport simulations of uranium in situ leaching : forecast and process optimization, in: Proceedings of the 7th International Conference on Uranium Mining and Hydrogeology, Freiberg, Germany.

Robin, V., Tertre, E., Beaufort, D., Regnault, O., Sardini, P., Descostes, M., 2015. Ion exchange reactions of major inorganic cations (H+, Na+, Ca2+, Mg2+ and K+) on beidellite: experimental results and new thermodynamic database. Towards a better prediction of contaminant mobility in natural environments. App. Geochem. 59, 74–84.

Robin, V., Tertre, E., Regnault, O., Descostes, M., 2016. Dissolution of beidellite in acidic solutions: new insights on interface reactions and effect of crystal chemistry on smectite reactivity. Geochim. Cosmochim. Acta. 180, 97–108. DOI 10.1016/j.gca.2016.02.009.

Robin, V., Tertre, E., Beaucaire, C., Descostes, M., Regnault, O., 2017. Experimental data and assessment of predictive modeling for radium ion exchange on swelling clay minerals with a tetrahedral charge. Appl. Geochem. 85, 1–9. DOI 10.1016/j.apgeochem.2017.07.009.

Robin, V., Beaufort, D., Tertre, E., Reinholdt, M., Fromaget, M., Forestier, S., de Boissezon, H., Descostes M., 2020. Fate of dioctahedral smectites in uranium roll front deposits exploited by acidic In Situ Recovery (ISR) solutions. Appl. Clays Sc. 187, article 105484.

Robinet, J.C., Sardini, P., Siitari-Kauppi, M., Prêt, D., Yven, B., 2015. Upscaling the porosity of the Callovo-Oxfordian mudstone from the pore scale to the formation scale; insights from the 3H-PMMA autoradiography technique and SEM BSE imaging, Sedim. Geol. 321 1-10

Sajih, M., Bryan, N.D., Livens, F.R., Vaughan, D.J., Descostes, M., Phrommavanh, V., Nos, J., Morris, K., 2014. Adsorption of radium and barium on goethite and ferrihydrite: a kinetic

and surface complexation modelling study. Geochim. Cosmochim. Acta. 146, 150–163. DOI 10.1016/j.gca.2014.10.008.

Sardini, P., Caner, L., Mossler, P., Mazurier, A., Hellmuth, K.-H., Graham, R.C., Rossi, A.M., Siitari-Kauppi, M., 2015. Calibration of digital autoradiograph technique for quantifying rock porosity using 14C-PMMA method. J. Radioanal. Nucl. Chem. 303 (1), 11–23. DOI 10.1007/s10967-014-3617-9.

Sardini, P., Angileri, A., Descostes, M., Duval, S., Oger, T., Patrier, P., Rividi, N., Siitari-Kauppi, M., Toubon, H., Donnard, J., 2016. Quantitative autoradiography of alpha particle emission in geo-materials using the Beaver^{TM} system. Nucl. Instrum. Methods Phys. Res. Sect. Accel. Spectrometers Detect. Assoc. Equip. 833, 15–22. DOI 10.1016/j.nima.2016.07.003.

Schmidt, C., Rufer, D., Preusser, F., Krbetschek, M., Hilgers, A., 2013. The assessment of radionuclide distribution in silex by autoradiography in the context of dose rate determination for thermoluminescence dating. Archaeometry 55(3), 407–422. DOI 10.1111/j.1475-4754.2012.00690.x.

Seredkin, M., Zabolotsky, A., Jeffress, G., 2016. In situ recovery, an alternative to conventional methods of mining: exploration, resource estimation, environmental issues, project evaluation and economics. Ore Geol. Rev. 79, 500–514. DOI 10.1016/j.oregeorev.2016.06.016.

Siiskonen, T., Pöllänen, R., 2005. Advanced simulation code for alpha spectrometry. Nucl. Instrum. Methods Phys. Res. Sect. Accel. Spectrometers Detect. Assoc. Equip. 550 (1–2), 425–434. DOI 10.1016/j.nima.2005.05.045.

Siitari-Kauppi, M., 2002. Development of 14C-Polymethylmethacrylate method for the characterisation of low porosity media: application to rocks in geological barriers of nuclear waste storage, PhD Dissertation, University of Helsinki, Helsinki, 2002.

Thers, D., Charpak, G., Coulon, P., Drancourt, C., Le Guay, M., Lupone, S., Luquin, L., Martínez, G., Meynadier, M., Pichot, P., 2003. Parallel Ionization Multiplier (PIM): a new concept of gaseous detector for radiation detection improvement. Nucl. Instrum. Methods Phys. Res. Sect. Accel. Spectrometers Detect. Assoc. Equip. 504, 161–165. DOI 10.1016/S0168-9002(03)00813-1.

WoldeGabriel, G., Boukhalfa, H., Ware, S.D., Cheshire, M., Reimus, P., Heikoop, J., Conradson, S.D., Batuk, O., Havrilla, G., House, B., 2014. Characterization of cores from an in-situ recovery mined uranium deposit in Wyoming: implications for post-mining restoration. Chem. Geol. 390, 32–45. DOI 10.1016/j.chemgeo.2014.10.009.

World Nuclear Association, 2018. In situ leach mining of uranium. http://www.world-nuclear.org/information-library/nuclear-fuel-cycle/mining-of-uranium/world-uranium-mining-production.aspx.

Yazikov, V.G, Zabaznov, V.U., 2002. Experience with restoration of ore-bearing aquifers after in situ leach uranium mining, in: Proceedings of The Uranium Production Cycle and the

Environment Conference, IAEA, 2nd-6th October 2002, Vienna, Austria. IAEA C&S Papers Series 10/P, pp 396–402.

Figure Captions

Figure 1: Bright field TEM of the thin section (Sample F) part showing UO_2 ilmenite and montmorillonite (a). HRTEM micrograph showing the fine microstructure of the particle, in inset the corresponding fast Fourier transform showing the ring pattern (b and 3). The particle diameter is around 100nm. In inset, the corresponding selected area diffraction shows ring pattern characteristic of a polycrystalline UO_2 particle. The size of the nanocrystals is around a few ten of nanometers.

Figure 2: Bright field TEM of the thin section (Sample L) part showing ilmenite and smectite (a). HRTEM micrograph showing the fine microstructure of the smectite, in inset the corresponding fast Fourier transform showing the ring pattern (b and 3). The particle diameter is around 100nm. The corresponding fast Fourier transform is shown in inset with d{001} ~ 10.4 Å.

Figure 3: Alpha map of (a) F and (b) L samples. Alpha activity is represented in grey scale. Black colour corresponds to a null alpha activity. In both samples the alpha activity is heterogeneous in spatial repartition, with hot spots of activity and areas of diffuse and null activity.

Figure 4: Alpha spectra of F (a) and L (b) samples. Grey line corresponds to the experimental alpha spectra and the black line is the simulation computed with AASI software

Figure 5: Plot diagram of size (X axis) versus activity (Y axis) for every hot spots on fresh (F, blue) and leached (L, red) samples.

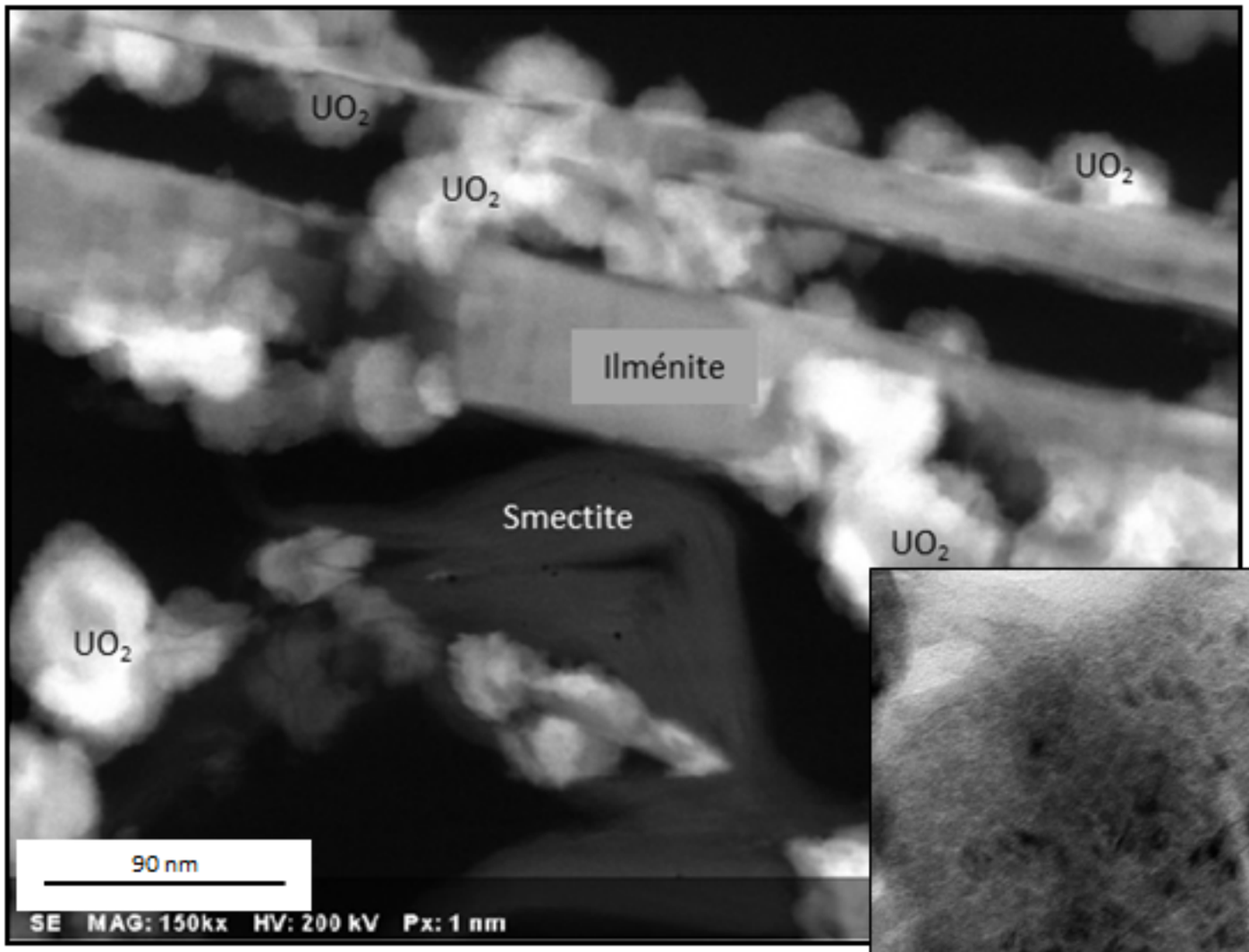

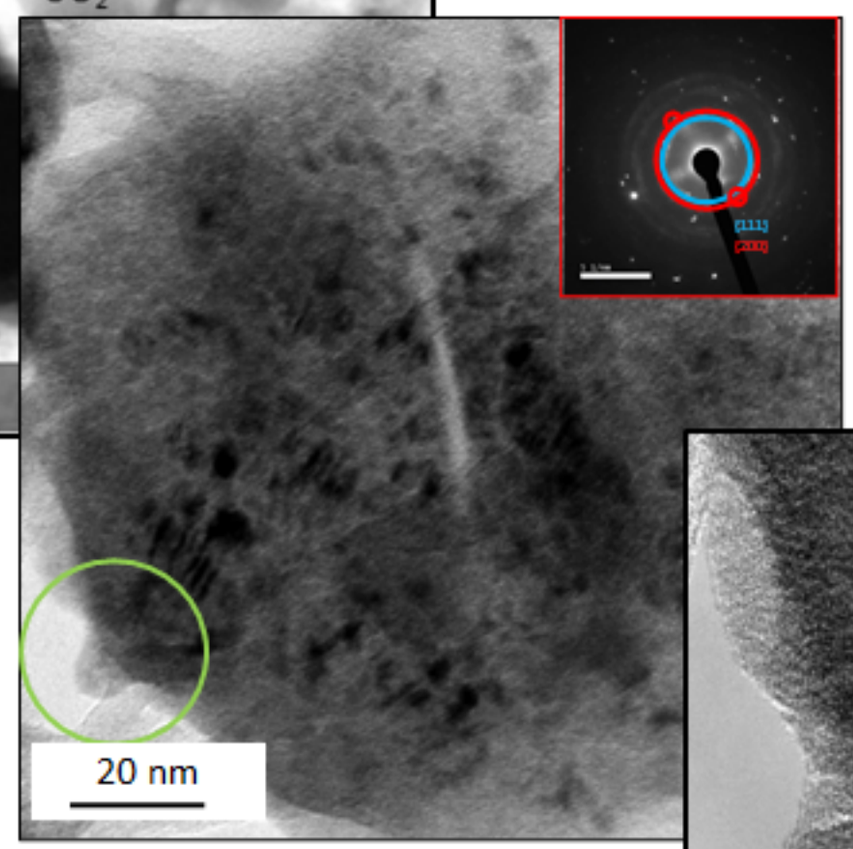

Uraninite : small crystallites

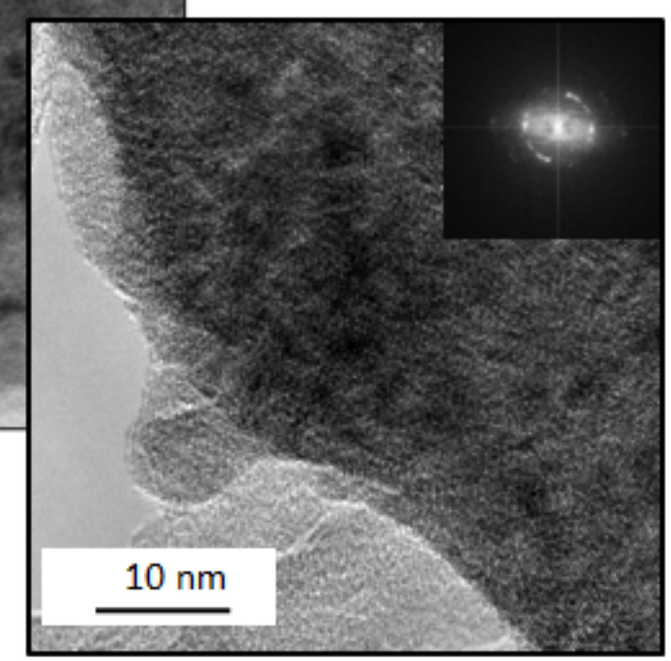

FFT – Ring {111}

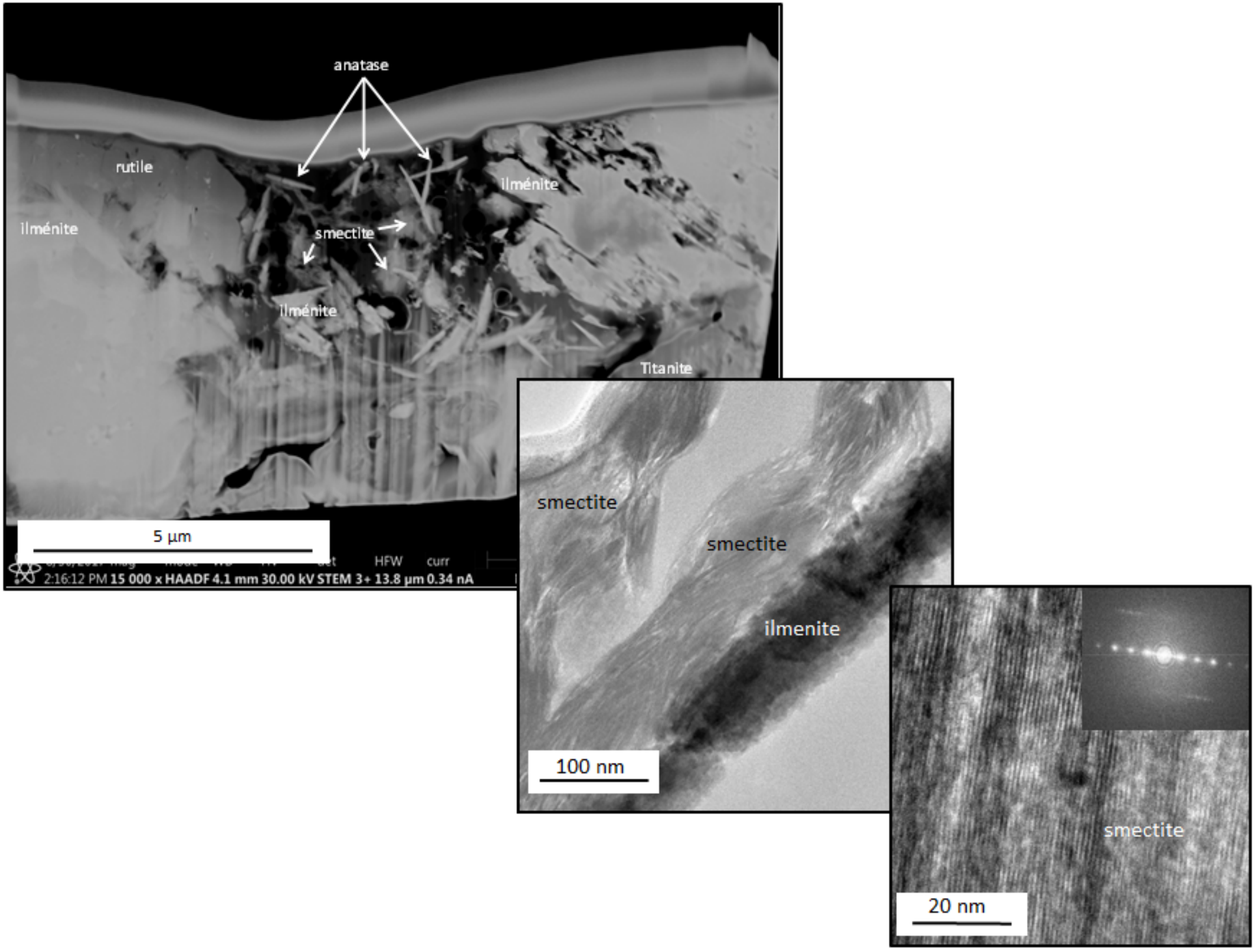
anatase
rutile
ilménite
ilménite
smectite
ilménite
Titanite
5 µm
HFW curr
2:16:12 PM 15 000 x HAADF 4.1 mm 30.00 kV STEM 3+ 13.8 µm 0.34 nA
smectite
smectite
ilmenite
100 nm
smectite
20 nm

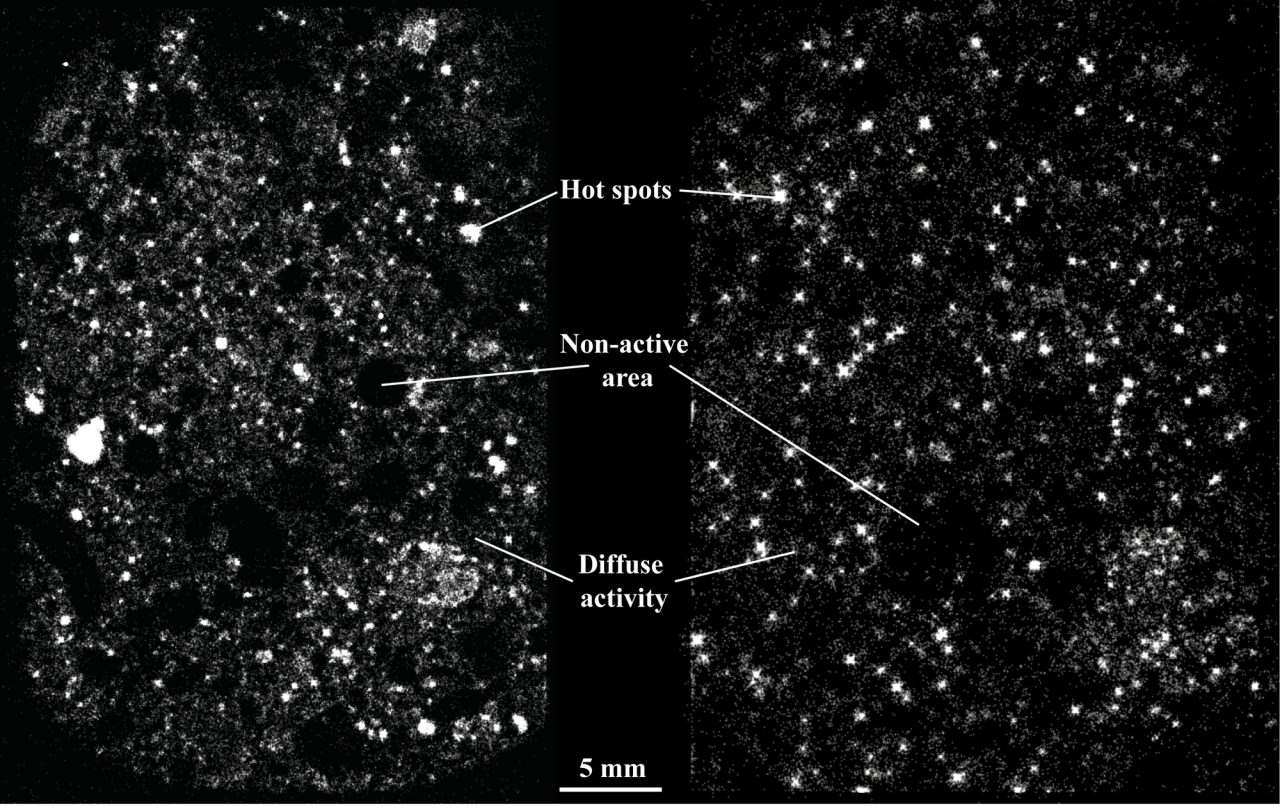

(a) (b)

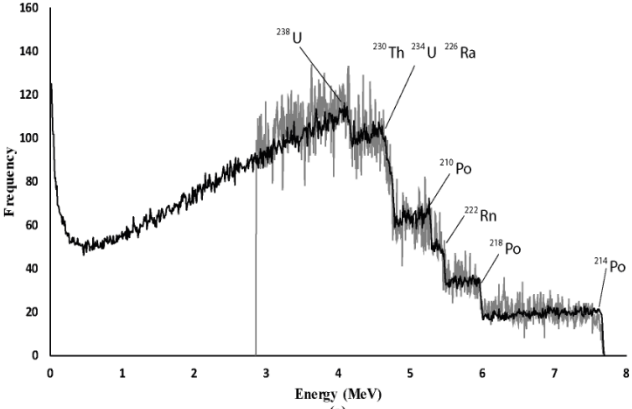
160
140
120
100
80
60
40
20
0
Frequency
0
1
2
3
4
5
6
7
8
Energy (MeV)
238U
230Th
234U
226Ra
210Po
222Rn
218Po
214Po

(a)

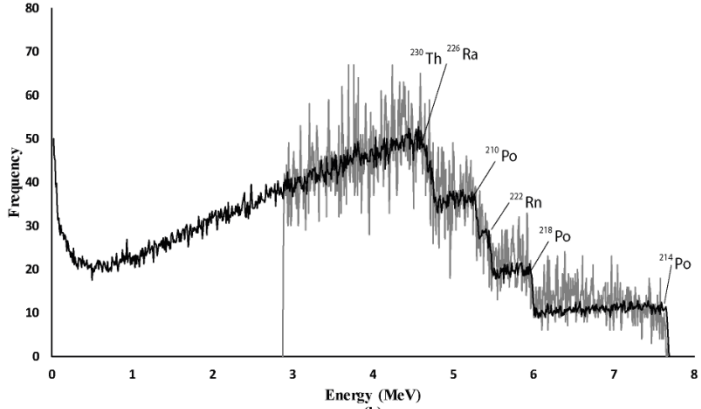
80
70
60
50
40
30
20
10
0
Frequency
0
1
2
3
4
5
6
7
8
Energy (MeV)
230Th
226Ra
210Po
222Rn
218Po
214Po

(b)

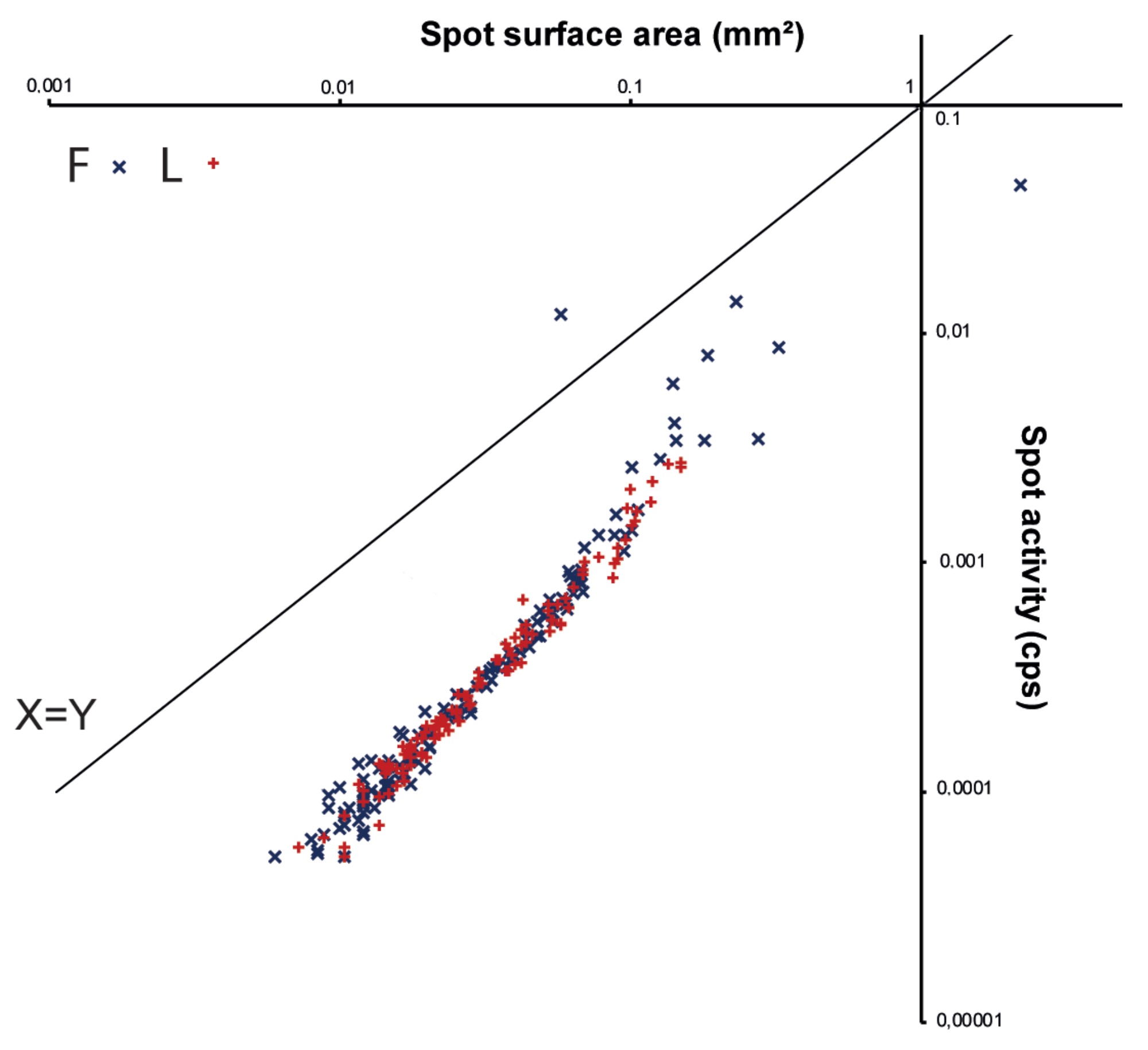
Spot surface area (mm²)
0.001
0.01
0.1
1
0.1
0,01
0.001
0,0001
0,00001
Spot activity (cps)
F
L
X=Y

Table 1

Alpha activity and activity contribution of alpha emitters in the ^{238}U decay chain for samples F and L. (1) Beaver activity; (2) Theoretical activity from U bulk content. Activities are related to bulk samples (whole-surface measurement for Beaver and bulk U concentration for theoretical activity).

	Alpha emission (cps/mm²)		Emission contribution of each alpha emitter in the 238U decay chain (%)							
Sample	(1)	(2)	^{238}U	^{234}U	^{230}Th	^{226}Ra	^{222}Rn	^{218}Po	^{214}Po	^{210}Po
F	9.3×10^{-4}	7×10^{-4}	12.5	12.5	12.5	12.5	12.5	12.5	12.5	12.5
L	2.3×10^{-4}	1.3×10^{-5}	0	0	16.6	16.6	16.6	16.6	16.6	16.6